Modeling Nonperturbative Field-Driven Vibronic Dynamics: Selective State Preparation and Nonlinear Spectroscopy

Modeling non-perturbative field-driven vibronic dynamics: Selective state preparation and nonlinear spectroscopy †

Justin Provazza,[‡] Francesco Segatta,[‡,¶] and David F. Coker[‡]

‡*Department of Chemistry, Boston University, 590 Commonwealth Avenue, Boston, Massachusetts 02215, USA*

¶*Dipartimento di Chimica Industriale "Toso Montanari", University of Bologna, Viale del Risorgimento, 4, 40136 Bologna, Italy*

E-mail:

Abstract

The partially linearized density matrix formalism for non-adiabatic dynamics is adapted to incorporate a classical external electromagentic field into the system Hamiltonian. This advancement encompasses the possibility of describing field-driven dynamics and compute a variety of linear and nonlinear spectroscopic signals beyond the perturbative limit. The capabilities of the developed approach are demonstrated on a simple two-state vibronic model coupled to a bath, for which we (a) perform an exhaustive search in the field parameter space for optimal state preparation and (b) compute time-resolved transient absorption spectroscopy to monitor the effect of different pulse shapes on measurable experimental signals. While no restrictions on the form of the field have to be assumed, we focus here on Gaussian shaped (linearly) chirped pulses.

[†]JP and FS contributed equally to this work.

1 Introduction

Interrogation of molecular systems with electromagnetic fields in the UV/VIS and IR spectral ranges represents a crucial mechanism for understanding and manipulating static and dynamical molecular properties. Light pulses can be tailored for the preparation of molecular systems in a desired state,[1] or to enhance a particular process[2] such as, for example, the guidance and localization of excitation energy in multi-chromophore complexes,[3] the elongation of excited state lifetimes *via* directed wave packet dynamics,[4,5] or controlling intramolecular vibrational energy redistribution.[6] Such manipulations can be experimentally implemented *via* closed-loop optimization techniques[7] that aim to maximize properties such as fluorescence yield,[8] isomerization reactions,[9,10] targeted excitation of a particular vibrational wave packet on an excited electronic surface,[11] or control the efficiency of photosynthetic complexes.[12] These experiments can be performed with little-to-no knowledge about the underlying molecular potential, leading to difficulties in the interpretation of the physical mechanisms behind the non-equilibrium dynamics which follows photo-excitation with the (often highly complicated) optimally tuned field.

Light pulses may also be used to monitor the non-equilibrium dynamical processes that occur following photo-activation of a molecular system by means of time-resolved spectroscopic techniques.[13–18] The interaction of the molecule(s) with an external field perturbs the molecular electron density, producing a time-dependent macroscopic polarization that gives rise to a new electric field that can be measured experimentally to reveal information about the molecular system itself. The recorded signals are often characterized by overlapping features, which makes it difficult to univocally interpret the photo-induced processes and unravel their microscopic origin.

In both cases, whenever light is used to control a given molecular property or to monitor a specific dynamical process, theoretical models are necessary to obtain a microscopic understanding of the triggered events and to properly interpret the measured signals.

Quantum optimal control theory has provided a theoretical framework whereby one solves

the Schrödinger equation iteratively while optimizing the form of the incident field to manipulate the molecular system in a way that enhances a particular process of interest. Synergy between theory and experiment on this front is bi-directional. On one end, theoretical models could suggest pulse shapes to be experimentally implemented, or potentially act as starting points for the closed-loop optimization scheme based on physical insight. On the other end, experimentally obtained optimized fields can be characterized and incorporated into quantum dynamical simulations with *ab initio* parameterized models of the molecular potential to aid in the interpretation of physical mechanisms underlying the optimized photo-excitation process.

Simulation of linear and nonlinear spectroscopy, which reduces to the computation of the time-dependent field-induced macroscopic polarization, has been accomplished by means of both perturbative and non-perturbative approaches. In the former case, the system response to the external perturbation is summarized in response functions that correspond to multi-point dipole autocorrelation functions. The response function formalism is well established and has been shown to be effective in many examples.[19–21] Nonetheless, there are cases in which one wishes to consider field-matter interactions that are stronger than those that can be concisely described by a perturbative expansion and thus are more adequately described through an explicit non-perturbative treatment of field-matter interactions.

The most general approach that allows one to deal with both the control over photo-induced dynamics and the simulation of spectroscopy beyond the perturbative limit, is that of treating explicitly the time-dependent field-matter interaction term in the Hamiltonian in dynamical simulations. To be effective, such an approach should combine an accurate description of the molecular system (i.e. a proper parameterization of the molecular potential) and an adequate dynamical method that is able to evolve the molecular degrees of freedom in presence and absence of an external driving field.[22,23] Such an effective methodology has been recently implemented in the framework of the partially linearized density matrix (PLDM) algorithm.

PLDM has been successfully applied to many problems in nonadiabatic dynamics such as photosynthetic excitation energy transfer,[24,25] electron transfer,[26] linear and nonlinear electronic spectroscopy (in the perturbative limit),[27] and cavity quantum electrodynamics,[28] among others. Moreover, a recently-developed spin coherent state-based PLDM algorithm has been presented that shows great promise for describing nonadiabatic processes.[29,30] Here, we describe the application of the PLDM algorithm for simulating field-driven dynamics beyond the perturbative limit, with the ultimate goal of characterizing the impact of shaped pulses on state preparation, non-equilibrium time-evolution of the molecular system, and simulation of linear and nonlinear electronic spectroscopy.

The outline of this paper is as follows: First we present the modifications that have been implemented in the PLDM methodology to explicitly include the time-dependent field-matter interaction term. Next we introduce and characterize the time-dependent electric field and its parameters, and show how its properties can be analyzed both theoretically and experimentally. Then we show the results obtained within a simple two-state vibronic model coupled to a bath, for which we exploit both the control capabilities, by performing an exhaustive search in the field parameter space for optimal state preparation, and the spectroscopic simulations of time-resolved transient absorption spectroscopy beyond the perturbative limit, to monitor the effect of different pulse shapes on the signals.

2 Theory

2.1 Partially linearized path integral dynamics of field-driven systems

The Schrödinger equation describing a quantum molecular system driven by a classical radiation field can be expressed as

$$i\hbar\frac{\partial\left|\psi\right\rangle}{\partial t}=\left(\hat{H}_{\mathrm{mol}}+\hat{H}_{F}(t)\right)\left|\psi\right\rangle \tag{1}$$

where $\hat{H}_{\text{mol}}$ is the molecular Hamiltonian describing the nuclear and electronic degrees-of-freedom (DOFs), and the field-matter interaction term is assumed to be given by $\hat{H}_F(t) = -\hat{\boldsymbol{\mu}} \cdot \boldsymbol{E}(t)$ where $\hat{\boldsymbol{\mu}}$ is the molecular dipole operator and $\boldsymbol{E}(t)$ is the incident electric field. We assume $\boldsymbol{E}(t)$ to be expressed as a sum of several phase-locked pulses, so that $\boldsymbol{E}(t) = \sum_{j=1}^{N_F} \boldsymbol{\epsilon}_j \tilde{E}_j(t-\tau_j)\cos(\omega_j(t-\tau_j)+\varphi_j(t-\tau_j))$, where $\boldsymbol{\epsilon}_j$, $\tilde{E}_j(t)$, ω_j, τ_j and $\varphi_j(t)$ are the polarization vector, the real-valued temporal envelope, the oscillatory frequency, the pulse time-center, and the (possibly time-dependent) phase for the jth pulse, respectively.

The Schrödinger equation can be formally solved resulting in $|\psi(t)\rangle = |\psi(0)\rangle - \frac{i}{\hbar}\int_0^t dt' \hat{H}(t')\,|\psi(t')\rangle$. Iteratively plugging this expression into itself for the definition of the wave function appearing in the integrand, then changing integration bounds appropriately with proper normalization, the time-evolved wave function is found to be

$$\begin{aligned} |\psi(t)\rangle &= \hat{U}(t)\,|\psi(0)\rangle \\ &= \mathcal{T} e^{-\frac{i}{\hbar}\int_0^t dt' \hat{H}(t')}\,|\psi(0)\rangle \end{aligned} \tag{2}$$

where $\mathcal{T}$ is the time-ordering operator that enforces causality in the time-dependent propagator. The time-ordered propagator is understood in the usual sense as an infinite product of infinitesimal propagators

$$e^{-\frac{i}{\hbar}\int_0^t dt' \hat{H}(t')}\,|\psi(0)\rangle = \lim_{N\to\infty} \prod_{j=0}^{N} \left(1 - \frac{i\epsilon}{\hbar}\hat{H}(t_j)\right)|\psi(0)\rangle \tag{3}$$

Here, $t_j = j\epsilon$ where $\epsilon = t/N$ is the infinitesimal time step. The time-ordering operator enforces that the terms in this product are ordered such that terms of earlier times (smaller j values) appear further to the right.

We are interested in obtaining an algorithm for computing the time-evolved density matrix, $\hat{\rho}(t) = |\psi(t)\rangle\langle\psi(t)|$, resulting from the time-dependent field driven Hamiltonian. We henceforth assume that the optical field can only drive transitions between the ground, and manifold of excited electronic states, and that the Condon approximation holds. Conse-

quently, the time-dependent field-driven molecular Hamiltonian is expressed in a diabatic representation as

$$\begin{aligned}\hat{H}_{\mathrm{mol}} + \hat{H}_F(t) = \sum_{I=1}^{D} \frac{\hat{P}_I^2}{2M_I} + V_0(\hat{\mathbf{R}}) + \sum_{\alpha,\beta=1}^{N_s} h_{\alpha\beta}(\hat{\mathbf{R}}) \left|\alpha\right\rangle \left\langle\beta\right| \\ - \sum_{\alpha=1}^{N_s} \boldsymbol{\mu}_{\alpha g} \cdot \boldsymbol{E}(t)(\left|\alpha\right\rangle \left\langle g\right| + \left|g\right\rangle \left\langle\alpha\right|)\end{aligned} \tag{4}$$

where α and β label excited diabatic electronic basis states, $|g\rangle$ labels 6the electronic ground state, and $(\hat{R}, \hat{P})$ represent phase space operators for the D nuclear DOFs, with corresponding masses M_I. Here $V_0(\hat{\mathbf{R}})$ is the electronic state independent part of the nuclear interaction potential, while $h_{\alpha\beta}(\hat{\mathbf{R}})$ are the nuclear configuration dependent electronic Hamiltonian matrix elements in the diabatic representation. To proceed, we consider the mapping representation for the discrete system projection operators,[31–33] which follows from a cartesian representation of the bosonic raising and lowering operators as $|\alpha\rangle \rightarrow \hat{a}_\alpha^\dagger = \frac{1}{\sqrt{2\hbar}}(\hat{q}_\alpha - i\hat{p}_\alpha)$.

The rotating wave approximation (RWA) is often introduced as an accurate approximation to the field-matter interaction term at frequencies resonant with electronic transitions.[34] Additionally, invoking the RWA allows a more simple analysis while making connection to experimental spectroscopic signals appearing in phase-matched directions.[20,27] We start by writing the typical oscillatory term from the incident field in complex form as $\cos(\omega t + \varphi(t)) = \frac{1}{2}(e^{i(\omega t+\varphi(t))} + e^{-i(\omega t+\varphi(t))})$, and subsequently ignore the rapidly oscillating terms in the interaction representation of the field-matter coupling portion of the Hamiltonian resulting in

$$\begin{aligned}\hat{H}_F^{\mathrm{RWA}}(t) &= -\frac{1}{2}\sum_{j=1}^{N_F} \boldsymbol{\mu}_{ge} \cdot \boldsymbol{E}_j(t) \left[e^{i(\omega_j t+\varphi_j(t))} \left|g\right\rangle \left\langle e\right| + e^{-i(\omega_j t+\varphi_j(t))} \left|e\right\rangle \left\langle g\right|\right] \\ &= -\sum_{j=1}^{N_F} \boldsymbol{\mu}_{ge} \cdot \left[\boldsymbol{E}_j^+(t) \left|g\right\rangle \left\langle e\right| + \boldsymbol{E}_j^-(t) \left|e\right\rangle \left\langle g\right|\right]\end{aligned} \tag{5}$$

where $\boldsymbol{E}_j^+(t) = \frac{1}{2}\boldsymbol{\epsilon}_j \tilde{E}_j(t) e^{i(\omega_j t+\varphi_j(t))}$ and $\boldsymbol{E}_j^-(t) = (\boldsymbol{E}_j^+(t))^* = \frac{1}{2}\boldsymbol{\epsilon}_j \tilde{E}_j(t) e^{-i(\omega_j t+\varphi_j(t))}$ define the

"positive" and "negative" parts of the electric field.

For a description of the time-evolution of such a system, we utilize the PLDM formalism which is based upon a semiclassical description of the projection operator mapping variables combined with a truncated Wigner (linearized) description of the bath DOFs.[24,35] The derivation of this approach for the Hamiltonian in Eq. (4) proceeds analogously to the case without a time-dependent driving field. Here, we simply present the final result with some remarks and refer the reader to previous work for more formal details.[24,25,36] The (n_f, n_f')-th element of the time-evolved reduced density matrix $\sigma(t)$ within the PLDM approximation is computed according to

$$\begin{aligned}\sigma_{n_f,n_f'}(t) \approx & \sum_{n_0,n_0'=1}^{N_s} \int d\bar{\mathbf{R}}_0 \frac{d\bar{\mathbf{P}}_1}{(2\pi\hbar)^D} \int \mathcal{D}\bar{\mathbf{R}}(\tau)\mathcal{D}\bar{\mathbf{P}}(\tau)\mathcal{D}\mathbf{Z}(\tau)\mathcal{D}\mathbf{Y}(\tau) \int \frac{d\vec{q}_0 d\vec{p}_0}{(2\pi\hbar)^{N_s}} \frac{d\vec{q'}_0 d\vec{p'}_0}{(2\pi\hbar)^{N_s}} \\ & \times \frac{1}{4\hbar^2}(q_t^{(n_f)} + ip_t^{(n_f)})(q_0^{(n_0)} - ip_0^{(n_0)})(q_0'^{(n_0')} + ip_0'^{(n_0')})(q_t'^{(n_f')} - ip_t'^{(n_f')})W^{(n_0,n_0')}(\bar{\mathbf{P}}_1, \bar{\mathbf{R}}_0) \\ & \times \mathcal{G}(\vec{q}_0,\vec{p}_0)\mathcal{G}(\vec{q'}_0,\vec{p'}_0)\; e^{\frac{i}{\hbar}\int_0^t d\tau \left[\dot{\bar{\mathbf{R}}}_\tau - \bar{\mathbf{P}}_\tau \cdot \mathbf{M}^{-1}\right]\cdot \mathbf{Y}_\tau} e^{-\frac{i}{\hbar}\int_0^t \left[\dot{\bar{\mathbf{P}}}_\tau + \nabla_{\mathbf{R}_\tau} V_0(\bar{\mathbf{R}}_\tau) + \nabla_{\mathbf{R}_\tau}\bar{h}_{\rm map}(\bar{\mathbf{R}}_\tau,\vec{q}_\tau,\vec{p}_\tau,\vec{q'}_\tau,\vec{p'}_\tau)\right]\cdot \mathbf{Z}_\tau}\end{aligned} \tag{6}$$

In the above expression, $\bar{\mathbf{R}} = (\mathbf{R} + \mathbf{R}')/2$ and $\mathbf{Z} = \mathbf{R} - \mathbf{R}'$ represent mean and difference variables for the nuclear path where $\mathbf{R}$ ($\mathbf{R}'$) labels the forward (backward) nuclear path. Analogous definitions exist for $\bar{\mathbf{P}}$ and $\mathbf{Y}$ for the mean and difference nuclear momentum paths. The average mapping Hamiltonian evaluated along the mean bath path is defined as $\bar{h}_{\rm map}(\bar{\mathbf{R}}_\tau, \vec{q}_\tau, \vec{p}_\tau, \vec{q'}_\tau, \vec{p'}_\tau) = \frac{1}{4\hbar}\sum_{\alpha,\beta=1}^{N_s} h_{\alpha\beta}(\bar{\mathbf{R}}_\tau)(p_{\alpha_\tau}p_{\beta_\tau} + q_{\alpha_\tau}q_{\beta_\tau} + p'_{\alpha_\tau}p'_{\beta_\tau} + q'_{\alpha_\tau}q'_{\beta_\tau})$. Finally, the functions $\mathcal{G}(\vec{q}_0,\vec{p}_0) = \exp[-\frac{1}{2\hbar}\sum_{\alpha=1}^{N_s} p_{\alpha_0}^2 + q_{\alpha_0}^2]$ and $W^{(n_0,n_0')}(\bar{\mathbf{P}}_1,\bar{\mathbf{R}}_0) = \int d\mathbf{Z}_0 \,\langle \bar{\mathbf{R}}_0 + \frac{\mathbf{Z}_0}{2}|\,\hat{\rho}_0^{(n_0,n_0')}\,|\bar{\mathbf{R}}_0 - \frac{\mathbf{Z}_0}{2}\rangle\, e^{-\frac{i}{\hbar}\bar{\mathbf{P}}_1^T\cdot\mathbf{Z}_0}$ (*i.e.* the partial Wigner transform of the initial density operator) provide a (quasi)probability distribution for initial phase space DOFs. This equation can be further simplified by analytically performing the bath difference phase space path integrals, resulting in δ-functional constraints over the bath mean phase space paths. The sole remaining integrations are over initial values of the system mapping and bath phase

space variables, giving the final result:

$$\sigma_{n_f,n'_f}(t) \approx \frac{1}{4\hbar^2}\sum_{n_0,n'_0=1}^{N_s}\int d\bar{\mathbf{R}}_0 \frac{d\bar{\mathbf{P}}_1}{(2\pi\hbar)^D}\int \frac{d\vec{q}_0 d\vec{p}_0}{(2\pi\hbar)^{N_s}}\frac{d\vec{q'}_0 d\vec{p'}_0}{(2\pi\hbar)^{N_s}}\; W^{(n_0,n'_0)}(\bar{\mathbf{P}}_1,\bar{\mathbf{R}}_0) \\ \times \mathcal{G}(\vec{q}_0,\vec{p}_0)\mathcal{G}(\vec{q'}_0,\vec{p'}_0)(q_t^{(n_f)}+ip_t^{(n_f)})(q_0^{(n_0)}-ip_0^{(n_0)})(q_0^{\prime(n'_0)}+ip_0^{\prime(n'_0)})(q_t^{\prime(n'_f)}-ip_t^{\prime(n'_f)}) \tag{7}$$

Implementation of this equation consists of performing the integration over initial conditions via a Monte Carlo sampling procedure[1], propagating the system and bath DOFs by integrating Hamilton's equations according to

$$\begin{aligned}
\dot{\bar{\mathbf{R}}}_\tau &= \mathbf{M^{-1}}\cdot\bar{\mathbf{P}}_\tau \\
\dot{\bar{\mathbf{P}}}_\tau &= -\nabla_{\mathbf{R}_\tau}V_0(\bar{\mathbf{R}}) - \nabla_{\mathbf{R}_\tau}\bar{h}_{\mathrm{map}}(\bar{\mathbf{R}}_\tau,\vec{q}_\tau,\vec{p}_\tau,\vec{q'}_\tau,\vec{p'}_\tau) \\
\dot{q}_{\gamma\tau} &= \frac{1}{\hbar}\sum_{\beta=1}^{N_s}h_{\gamma\beta}(\bar{\mathbf{R}}_\tau)p_{\beta_\tau} + \frac{1}{\hbar}\left\{\mathrm{Re}\left[H_{F_{\gamma g}}^{\mathrm{RWA}}(\tau)\right]p_{g_\tau} + \mathrm{Im}\left[H_{F_{\gamma g}}^{\mathrm{RWA}}(\tau)\right]q_{g_\tau}\right\} \\
\dot{p}_{\gamma\tau} &= -\frac{1}{\hbar}\sum_{\beta=1}^{N_s}h_{\gamma\beta}(\bar{\mathbf{R}}_\tau)q_{\beta_\tau} - \frac{1}{\hbar}\left\{\mathrm{Re}\left[H_{F_{\gamma g}}^{\mathrm{RWA}}(\tau)\right]q_{g_\tau} - \mathrm{Im}\left[H_{F_{\gamma g}}^{\mathrm{RWA}}(\tau)\right]p_{g_\tau}\right\},
\end{aligned}$$

and finally computing the trajectory's contribution to the (n_f, n'_f)-th element of the time-evolved reduced density matrix according to Eq. (7). We have used the skew symmetry of $\mathrm{Im}\left[H_F^{\mathrm{RWA}}(\tau)\right]$ in the expressions for the propagation of mapping variables given above. There are analogous definitions for the time-evolution of the "backward" mapping variables, $q'_{\gamma\tau}$ and $p'_{\gamma\tau}$. Similar expressions describe the time-evolution of mapping variables that represent the ground electronic state.

From a numerical integration standpoint, implementation of the RWA is highly advantageous. For the electronic excitations of interest to this work (generally on the order of

[1]The mapping variables are most efficiently sampled by transforming into polar coordinates and sampling the radial cumulant directly and the angle uniformly $\in (0, 2\pi]$. With this procedure, one can include the initial polynomial term into the sampling distribution so the initial trajectory weight is a complex number that is ensured to carry unit magnitude. On the other hand, simply sampling the positive-definite Gaussian term in cartesian space, such as $\mathcal{G}(\vec{q}_0,\vec{p}_0)$, and weighting each trajectory by the initial polynomial term results in frequent computation of trajectories that contribute little to the ensemble, giving a poorly convergent algorithm.

10^4 cm^{-1}) the RWA, which we implement in a rotating frame, provides an avenue for retaining accuracy while allowing one to artificially decrease the energy gap between the ground and excited state manifolds. This, in turn, allows one to reduce the number of samples needed to properly describe the time-dependent field, and thus update the field matter interaction term in the Hamiltonian less frequently while numerically integrating Hamilton's equations as described above, leading to negligible additional numerical effort when compared to propagation with time-independent Hamiltonians. For a more complete description of the numerical benefits of invoking the RWA, we refer the reader to the Supporting Information.

2.2 Field Design and Characterization

Implementation of PLDM field-driven dynamics as described above does not require any constraint on the form of the incident electric field. Nonetheless, for simplicity, we focus on Gaussian shaped (linearly) chirped pulses. We therefore have that

$$\boldsymbol{E}^{+}(t) = \boldsymbol{\epsilon}\frac{1}{2}\lambda_F e^{-t^2/2\sigma_t^2} e^{i\left(\omega t + at^2 + \phi\right)} \tag{8}$$

where λ_F is the field amplitude, and σ_t controls the temporal width of the pulse. The quadratic term in the complex exponential is responsible for the linear chirp of the pulse, which provides a different temporal ordering of the pulse frequency components: when the chirp coefficient, a, is positive, the low frequency components reach the sample before the high frequency components, whereas for a negative chirp the order is reversed. A discussion of the constant phase, ϕ, which arises from the wave-vector spatial part of the field in the dipole approximation is presented below.

The pulse can be characterized in both the time domain and the frequency domain (related through their Fourier transforms). The former highlights the time-center of the pulse and its width in time, while the latter reveal the frequency components spanned by the pulse. A mixed time-frequency representation, that simultaneously gives the temporal

and frequency dependence of the field, is also possible.[37] One such representation is provided by the Wigner spectrum of the field, defined as[38]

$$W(t,\Omega) = \int_{-\infty}^{\infty} ds\ E^{+}\left(t+\frac{s}{2}\right) E^{+*}\left(t-\frac{s}{2}\right) e^{-i\Omega s} \tag{9}$$

The Wigner spectrum allows one to visualize the temporal-spectral correlation of the incident radiation field, providing a useful way to interpret the impact a field may have on a molecular system. Among its properties, the marginals of the Wigner distribution are directly related to the intensity profile of the field in both the time and the frequency domain.

The field is also labeled by a wave-vector $\mathbf{k}$, that enters as a phase factor given by $e^{i\mathbf{k}\cdot\mathbf{r}}$. When dealing with nonlinear spectroscopy simulations, where multiple laser field beams interact with the sample, impinging at different angles, signals of different types may be recorded in different (so called phase-matched) directions that correspond to particular linear combinations of the incident field wave-vectors.

3 Applications

Useful applications of the field-driven dynamics extension of the PLDM algorithm include: control over state preparation, and nonlinear spectroscopy simulations beyond the perturbative limit. Here, we discuss the basic ingredients that are needed to address these two tasks, while reporting practical examples in the Section 4.

3.1 Selective State Preparation

The ability to selectively prepare a molecular system in some predefined region of state space, $\mathcal{H}_\chi$, through strategically designed quantum quench processes is a crucial step toward practical application of quantum optimal control theory.[2] In the context of the preparation of particular vibronic states through linearly chirped electromagnetic pulse interactions, as defined in Eq. (8), the goal is to identify the set of field parameters that optimizes the

preparation of a specific target density as

$$\boldsymbol{E}_{\text{opt}}(t) = \left\{ \boldsymbol{E}(t;\omega,\lambda_F,\sigma_t,a) \middle| \langle m| \left(\hat{\sigma}(t) - \hat{\chi}\right) |n\rangle = 0 \;\forall\; m,n \in \mathcal{H}_\chi \right\} \tag{10}$$

where $\hat{\chi}$ is a projection operator corresponding to the target state density (or coherence) in the Hilbert subspace of the system, $\mathcal{H}_\chi$. We have highlighted the parametric dependence of the varied field on the parameters defining the linearly chirped pulse. For multi-pulse sequences, one must also consider time delays between pulse centers as additional parameters for the definition of the optimal electric field. In practice, the optimal pulse is determined as the pulse that most closely satisfies the equality defined in Eq. (10) and, in general, it is not unique.

3.2 Non-Perturbative Pump Probe Spectroscopy

One particularly insightful avenue for making connection with experimental measurements is provided by the calculation of time-resolved nonlinear electronic spectroscopy signals that report on the evolution and relaxation processes of non-equilibrium state preparations.[39] While one can, in the weak-field limit, accurately calculate the nonlinear polarization of a molecular system within the response function formalism,[19,20,27] there are situations in which a non-perturbative treatment can be advantageous. For example, when interested in the polarization induced by fields with overlapping temporal envelopes, the non-perturbative analysis is more straightforward.[40–42] One highly efficient method for extracting the nonlinear polarization signals in phase-matched directions arising from non-perturbative field-matter interactions involves the non-Hermitian propagation of a limited set of auxiliary density matrices.[43–45] Propagation of the density matrix with the PLDM algorithm, however, is not amenable to non-Hermitian Hamiltonians, forcing us to consider an alternative route: this was first designed by Domcke and collaborators for (third-order) pump-probe spectroscopy,[40] and then extended to 2DES.[42] In this study we will consider the PLDM implementation of

non-perturbative pump-probe spectroscopy.

The experimental setup consists of two incident radiation fields, a "pump" pulse defined by $\mathbf{E}_1(t-\tau_1)$ with wave vector $\mathbf{k}_1$, and a "probe" pulse defined by $\mathbf{E}_2(t-\tau_2)$ with wave vector $\mathbf{k}_2$. The pump and probe pulses are temporally separated by an amount $\tau_2 - \tau_1 = \Delta t$. In such experiments, the pump pulse is chosen to be sufficiently strong such that the field-matter interaction produces population in the excited electronic state, thus creating and out-of-equilibrium wave-packet whose evolution is monitored by the (weaker) probe pulse. The total polarization induced in the molecular system by the pair of pulses, is given by $\mathbf{P}(t) = \mathrm{T}r[\hat{\boldsymbol{\mu}}\hat{\rho}(t)]$. This polarization contains contributions from different orders of interaction between the incident field and the system, and for isotropic samples it can be expanded in an odd-order series as

$$\mathbf{P}(t) = \sum_{n=0}^{\infty} \mathbf{P}^{(2n+1)}(t) \tag{11}$$

where $\mathbf{P}^{(N)}(t)$ is the Nth order polarization, and in the isotropic case all even-order terms vanish. While in the weak-field (*i.e.* perturbative) regime it is possible to directly access the desired polarization order (as, e.g., $\mathbf{P}^{(1)}(t)$ for linear spectroscopy and $\mathbf{P}^{(3)}(t)$ for pump-probe and 2D), the problem of how to separate a particular contribution from the total polarization has to be addressed for our non-perturbative approach. Experimentally, such a separation between first and third-order techniques (third order being the lowest order non-vanishing nonlinear polarization) is achieved by (i) considering sufficiently weak fields such that higher-order interactions between the field(s) and the molecular system can be safely neglected, and (ii) recording the signal in particular directions, which are known to be specific for given first or third-order spectroscopic techniques.[19] This well established approach is understood in the context of the RWA, for which it can be demonstrated that the response for the third-order polarization signal, $\mathbf{P}^{(3)}(t)$, radiates in the phase matched directions $\mathbf{k}_1$, $\mathbf{k}_2$, $2\mathbf{k}_2 - \mathbf{k}_1$, and $2\mathbf{k}_1 - \mathbf{k}_2$.

From the theoretical point of view, following the approach of Ref. 40, it is possible to extract the different phase-matched signals from the total polarization by a careful selection and combination of the phase-locked conditions between the pump and probe pulses. When the pulses are phase-locked relative to each other, the complex polarization up to third-order can be expressed as

$$\mathbf{P}_t(\phi) = \sum_n \mathbf{P}_n(t) e^{in\phi} \tag{12}$$

where n represents the four different directions in which the polarization radiates.[2] Choosing $n\phi = n\mathbf{k}_1 \cdot \mathbf{r}$, the four directions can be separated by computing the overall polarization $\mathbf{P}_t(\phi)$ with $\phi = m\pi/2$ for $m \in [0, 3]$.[43,44] From here, the directional components of the polarization can be extracted as[40]

$$\begin{aligned}
\mathbf{P}_{\mathbf{k}_2}(t) &= \frac{1}{4}\Big(\mathbf{P}_t(0) + \mathbf{P}_t(\pi/2) + \mathbf{P}_t(\pi) + \mathbf{P}_t(3\pi/2)\Big) \\
\mathbf{P}_{\mathbf{k}_1}(t) &= \frac{1}{4}\Big(\mathrm{Re}\{\mathbf{P}_t(0) - \mathbf{P}_t(\pi)\} + \mathrm{Im}\{\mathbf{P}_t(\pi/2) - \mathbf{P}_t(3\pi/2)\}\Big) \\
&\quad + i\frac{1}{4}\Big(\mathrm{Im}\{\mathbf{P}_t(0) - \mathbf{P}_t(\pi)\} + \mathrm{Re}\{\mathbf{P}_t(3\pi/2) - \mathbf{P}_t(\pi/2)\}\Big) \\
\mathbf{P}_{2\mathbf{k}_2-\mathbf{k}_1}(t) &= \frac{1}{4}\Big(\mathrm{Re}\{\mathbf{P}_t(0) - \mathbf{P}_t(\pi)\} + \mathrm{Im}\{\mathbf{P}_t(3\pi/2) - \mathbf{P}_t(\pi/2)\}\Big) \\
&\quad + i\frac{1}{4}\Big(\mathrm{Im}\{\mathbf{P}_t(0) - \mathbf{P}_t(\pi)\} + \mathrm{Re}\{\mathbf{P}_t(\pi/2) - \mathbf{P}_t(3\pi/2)\}\Big) \\
\mathbf{P}_{2\mathbf{k}_1-\mathbf{k}_2}(t) &= \frac{1}{4}\Big(\mathbf{P}_t(0) - \mathbf{P}_t(\pi/2) + \mathbf{P}_t(\pi) - \mathbf{P}_t(3\pi/2)\Big)
\end{aligned}$$

In practice, the complex polarizations $\mathbf{P}_t(\phi)$ are computed by adding a constant phase, ϕ, to the pump pulse, which takes the form $\mathbf{E}_1(t-\tau_1)e^{i\phi}$, while ϕ is kept fixed to zero for the probe pulse in all calculations. Four different sets of $\mathbf{P}_t(\phi)$ computations are performed for the four values of ϕ, and combined in the manner described above to extract a specific phase-matched contribution to the polarization. In order for such an approach to be effective, the RWA must hold, and the field strength should remain weak enough that higher-order field-matter interactions (*e.g.* 5th and higher order interactions) are negligible in the total

[2]The total real-valued polarization is related to this expression as $\mathbf{P}_t^{\mathrm{tot}}(\phi) = \mathbf{P}_t(\phi) + \mathbf{P}_t^*(\phi)$.

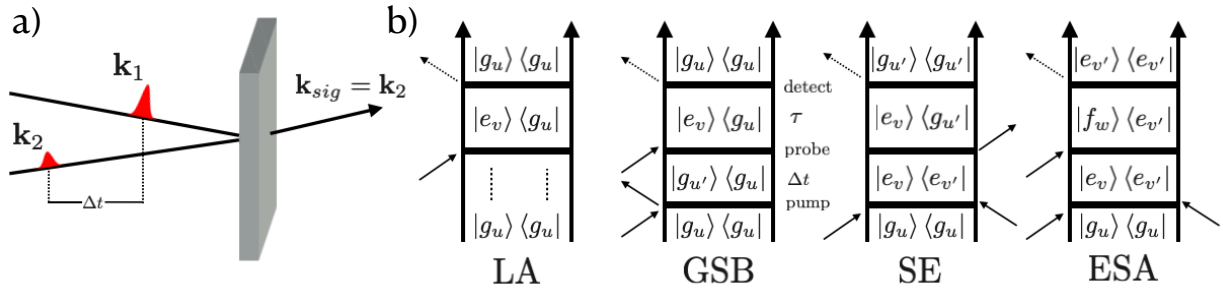

Figure 1: Figure (a) depicts a general schematic of a pump-probe experiment resulting in the signal that is radiated in the direction $\mathbf{k}_2$. Figure (b) shows the double-sided Feynman diagrams that contribute to this signal. The diagrams consist of linear absorption, ground state bleaching, stimulated emission, and excited state absorption. For the third-order contributions, GSB, SE, and ESA, the pump pulse interacts twice with the molecular system, preparing electronic ground state and excited state population. The molecular system then evolves until it interacts with the probe pulse, and finally emits a response. Here, Δt corresponds to the difference between the central times of the probe and pump pulses while τ corresponds to the difference between when the signal is measured and the central time of the probe pulse. The thick horizontal lines separating temporal domains of the Feynman diagrams illustrate that there is a finite temporal width associated with the incident laser pulses.

polarization.

We are interested in monitoring the signals that arise from systems that are prepared in populations by a shaped, and possibly chirped, pump pulse. These signals appear in the $\mathbf{k}_2$ direction, as illustrated in Figure 1. In this direction, there are three contributing processes. In the weak-field limit, the dominant signal will arise from linear absorption of the probe pulse. For third-order interactions, the contributions consist of the GSB process, in which the pump pulse prepares a ground electronic state population, and the SE process, in which the pump pulse prepares an excited electronic state population. The linear absorption signal is subtracted from the overall polarization to ensure that the signal recorded in the $\mathbf{k}_2$ direction is not dominated by the first order contribution.[3]

[3]It is worth mentioning that in the non-overlapping pulse regime, when one wishes only to differentiate the signal in the $\mathbf{k}_2$ from all the other signals, only two phase-locked total polarization calculations are required.[40]

4 Results

4.1 Shaped Pulses for Selective State Preparation

A simple approach to determine the optimal field for enhancing the preparation of a molecular state, as defined in Eq. 10, is to perform an exhaustive scan over the field parameter space and isolate the set of parameters that maximize the projection onto the state of interest. In Figure 2, results from a scan over values of carrier frequency, ω_c, temporal width σ_t, and the linear chirp parameter, a, for a simple vibronic model are reported. The molecular system is modeled by a one-dimensional spin-boson with a vibrational frequency of $\Omega = 500$ cm^{-1}, the Huang-Rhys factor is chosen as $S = 2$, and the vertical excitation energy is set to 5600 cm^{-1}. The field-matter Hamiltonian is defined by $\langle g, v_g | \hat{H}_F^{\mathrm{RWA}}(t) | e, u_e \rangle = \lambda_F \langle v_g | u_e \rangle e^{i(\omega_c(t-\tau)+a(t-\tau)^2)} e^{-\frac{(t-\tau)^2}{2\sigma_t^2}}$ with $\lambda_F = 400$ cm^{-1}, and $\langle v_g | u_e \rangle$ is the vibrational wave function overlap, or Franck-Condon, factor. In order to retain an accurate description of the vibronic system, the vibrational DOF is quantized and the resulting vibronic basis is represented with mapping variables for implementation of the PLDM algorithm.[27,46,47]

We choose to perform the scan to identify the set of field parameters that maximizes the production of vibrational excitation on the ground electronic state surface. In this case, the optimal field is found to have a carrier frequency of $\omega_c = 4600$ cm^{-1}, rather than the frequency resonant with the vertical transition, 5600 cm^{-1}. This is because the transition between ground vibrational states on each electronic surface is 4600 cm^{-1}, and since the optimal pulse turns out to be negatively chirped, it is subsequently able to pull population down into the vibrationally excited ground electronic state. This phenomenon has been detailed in a previous study involving shifted anharmonic potentials where nonequilibrium excited state wave packet dynamics drives the system toward configurations with redshifted electronic transition resonance conditions.[48]

Figure 2a reports the total population of vibrational excitation in the ground electronic state following the interaction of the one-dimensional spin-boson with the radiation field over

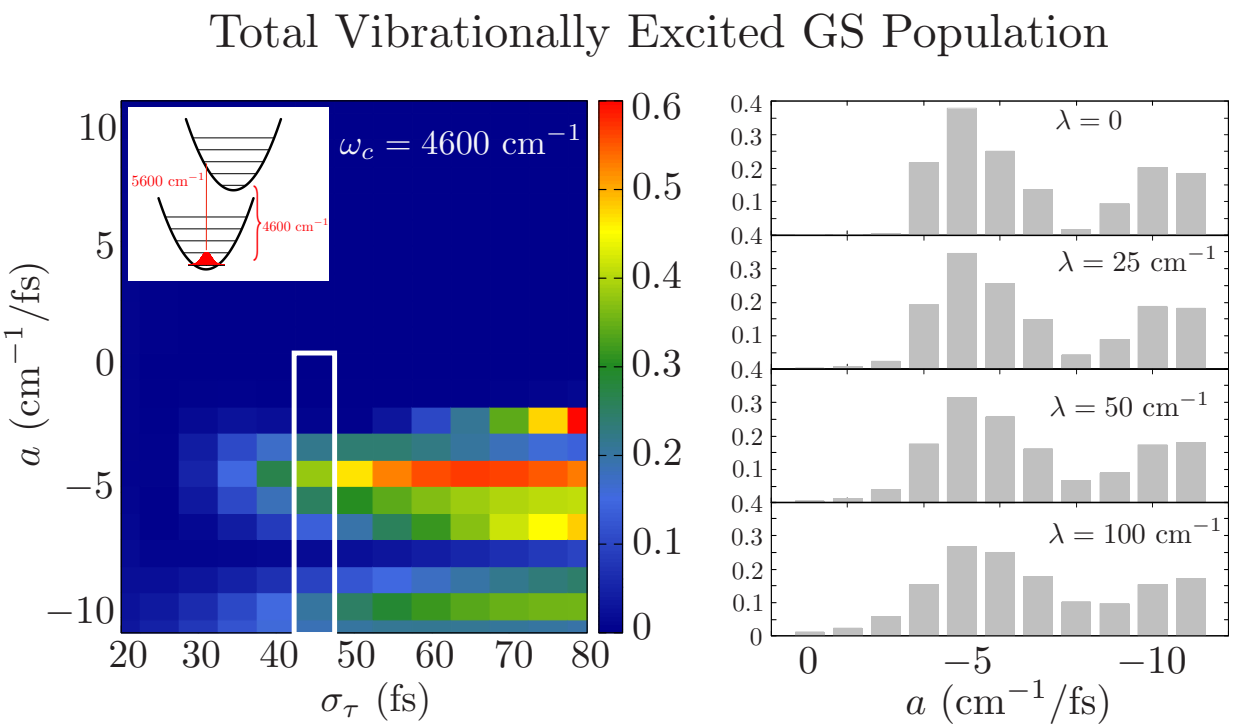

Figure 2: (a) Scan over Gaussian field parameters σ_τ, and a, for determining the optimal pulse to maximize the population of "hot" vibrational states in the ground electronic state with $\omega_c = 4600$ cm^{-1}. The molecular system was prepared in the ground electronic state and ground vibrational state before the field interaction, as illustrated in the inlay on the heat-map. The white rectangle outlines a range of parameters over which the population of vibrational excitatation in the ground state was examined in (b) with the addition of a linearized bath with varying reorganization energy, $\lambda = \frac{1}{\pi}\int_0^\infty d\omega \frac{J(\omega)}{\omega}$, at a temperature of 77 K.

a range of Gaussian temporal widths and linear chirp parameters. The "total vibrationally excited GS population" is defined as the sum of the vibrationally excited state populations on the ground state electronic potential surface after the pulse no longer interacts with the system. The resulting highly-structured heat-map highlights the sensitivity of this measure to the parameters of the field. Note, for example, the presence of specific chirp parameters that enhance ($a \sim -4.5$ cm^{-1}/fs), or suppress ($a \sim -7.5$ cm^{-1}/fs) the production of vibrationally excited GS population, as a result of the complicated relation between the arrival time of a given frequency component of the field and the present and past field-induced system dynamics. Similarly structured heat-maps, obtained at different values of the central frequency ω_c are reported in the supporting information.

The scan over parameters outlined above was performed in the absence of coupling to any bath DOFs. Figure 2(b), on the other hand, explores the impact of including a bath of harmonic oscillators coupled bilinearly to the excited electronic state. A vertical cut of the scan was considered, as highlighted by the white-edged rectangle of Figure 2(a), and system-bath coupling strengths over a range typical for bio-molecular energy transfer systems were explored.[25] A Drude-Lorentz spectral density, defined as

$$J(\omega) = 2\lambda \frac{\omega\gamma}{\gamma^2 + \omega^2} \tag{13}$$

was employed in these studies. We set the so-called dephasing or correlation time to $\gamma^{-1} = 50$ fs,[4] while λ, the reorganization energy, was varied from 0 to 100 cm^{-1}. It is interesting to notice how the highly structured profile of the total vibrationally excited GS population along the chirp coordinate (clearly visible for $\lambda = 0$ cm^{-1}), is smoothed out as λ is increased. This can be understood as an effect of the bath induced fluctuations in the GS and ES energy gap, that may spoil the perfect (but fragile) synchronization between the arrival of given frequency components of the pulse and the wave-packet position in time.

In Figure 3, we consider state preparation induced by two different example fields in the white-edged rectangle of Figure 2: an unchirped Gaussian pulse with $\sigma_t = 45$ fs, and a chirped Gaussian pulse with $a \sim -4.5$ cm^{-1}/fs and the same pulse width σ_t. In the limit of zero system-bath coupling ($\lambda = 0$ cm^{-1}), it was found for this model that the unchirped Gaussian pulse prepared the vibrational ground state in the excited state potential. This is because the pulse arrives with a carrier frequency that is resonant with the transition to this particular state, with a narrow enough frequency distribution that it does not strongly overlap with any vibrationally excited states on the ES potential. The negatively chirped pulse, however, contains more frequency components[5], and is able to produce an excited

[4]Here we choose to fix γ to a reasonable value without studying its impact on the proposed experiments. Such a study is feasible using the formalism developed here, and may prove interesting, as this parameter has been demonstrated to be an important factor influencing the control mechanism.[1]

[5]Note that, in Figure 2, different frequency axes are employed for the Wigner spectra of the unchirped and chirped pulses.

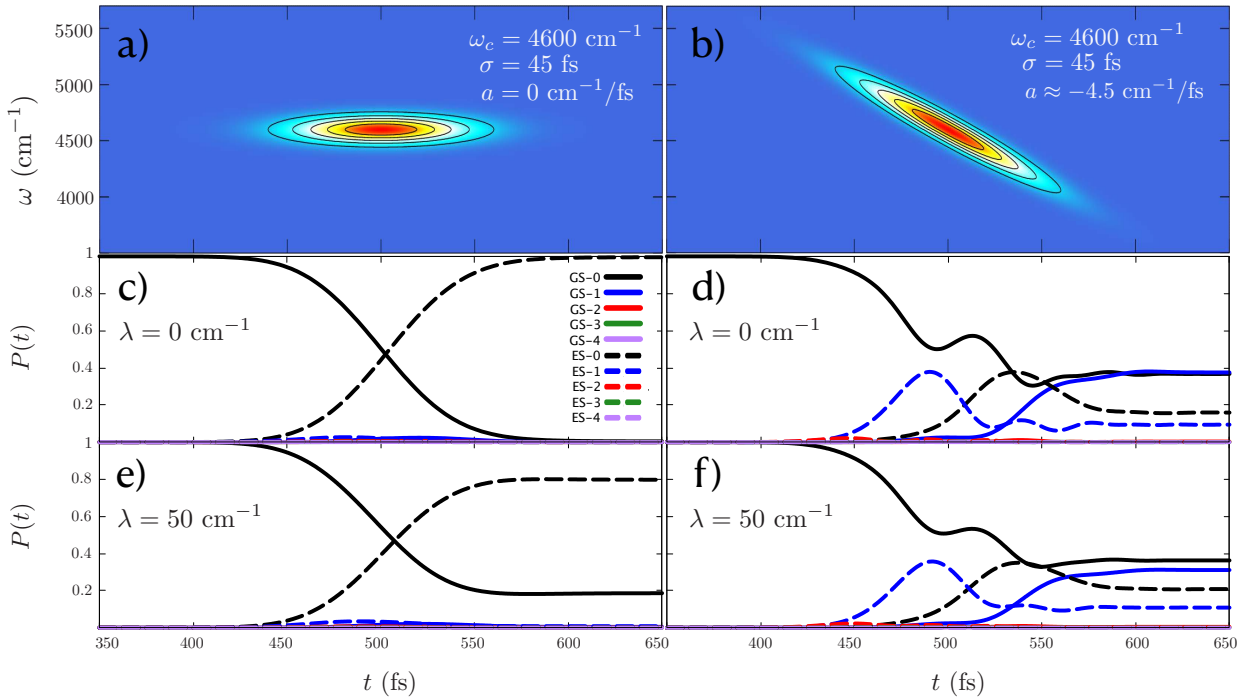

Figure 3: Wigner spectrum and state preparations for two fields from the scan in Figure 2. The panels (a),(c), and (e) on the left represent the unchirped Gaussian pulse and the vibronic states prepared through its interaction with the shifted harmonic system. The panels (b), (d), and (f) on the right represent a negatively chirped Gaussian pulse and the vibronic states prepared through its interaction with the shifted harmonic system. In the lower panels we plot vibronic state populations as functions of time during the interaction of the system with the pulses. Solid curves label the ground electronic populations and dashed curves label the excited electronic state populations. Different colored curves label the different excited vibrational states on each electronic surface with $v = 0$ (black), $v = 1$ (blue), and $v = 2$ (red). The results presented here involve preparing the system and its environment at a temperature of 77 K

vibrational wave packet as a linear combination of the ground and first excited oscillator states in both the ground and excited electronic state potentials. The inclusion of a non-zero system-bath coupling ($\lambda = 50$ cm^{-1}) is again shown to affect the state preparation, by (i) diminishing the amount of ES population that the unchirped pulse is able to produce, and (ii) reducing the ratio between cold and hot vibration populations in both the GS and ES electronic states.

4.2 Pump-Probe Spectroscopy with Shaped Pulses

As a proof-of-concept exploring the influence of pump-pulse shaping, we performed pump-probe spectroscopy calculations for the same one-dimensional spin-boson model described above, employing the two different fields used to generate the results reported in Figure 3 as pump pulses. The same probe pulses were used in both simulations, *i.e.* simple Gaussian shaped probe pulses with full-width-half-maximum of $2.355\sigma_\tau = 10$ fs, carrier frequency of $\omega_c = 4600$ cm^{-1}, and field-matter interaction strength of $\lambda_F = 100$ cm^{-1}. The spectroscopy simulations were conducted by implementing the approach of Reference 40, as described in Section 3.2, and the calculated pump-probe spectra we obtained are presented in Figure 4. For these calculations, "focused" initial conditions were implemented to limit the statistical noise as described in Reference 27.

The pump-probe signals reported in Figure 4 were obtained by first taking the Fourier transform of the polarization, $\mathrm{P}_{\mathbf{k}_2}(t)$, defined under Eq. (12) with respect to τ, the waiting time after the probe pulse, for each pump-probe delay time, Δt. The final plotted pump-probe signals are then obtained as the negative of the imaginary part of these Fourier transformed results. The left panels, Figure 4 (a) and (c), which corresponds to the unchirped simple Gaussian pump pulse, display no oscillatory behavior as a function of Δt. This is because the pump pulse, as indicated in Figure 3, prepares only the ground vibrational state in the excited state potential. Comparing the upper and lower sets of panels in Figure 4 explores the influence of the environmental bath that is coupled with different strengths, λ, only to the electronic states in our model.

The right panels, Figure 4 (b) and (d), on the other hand correspond to the negatively chirped Gaussian pulse, and display strong oscillatory behavior as a function of Δt. These oscillations arise because of the linear combination of ground and first excited vibrational states that this chirped pump pulse prepares on each electronic state potential surface (see Figure 3). The non-stationary linear combinations of excited vibrational states prepared by the chirped pump pulse oscillate at the vibrational frequency $\Omega = 500$ cm^{-1} (period

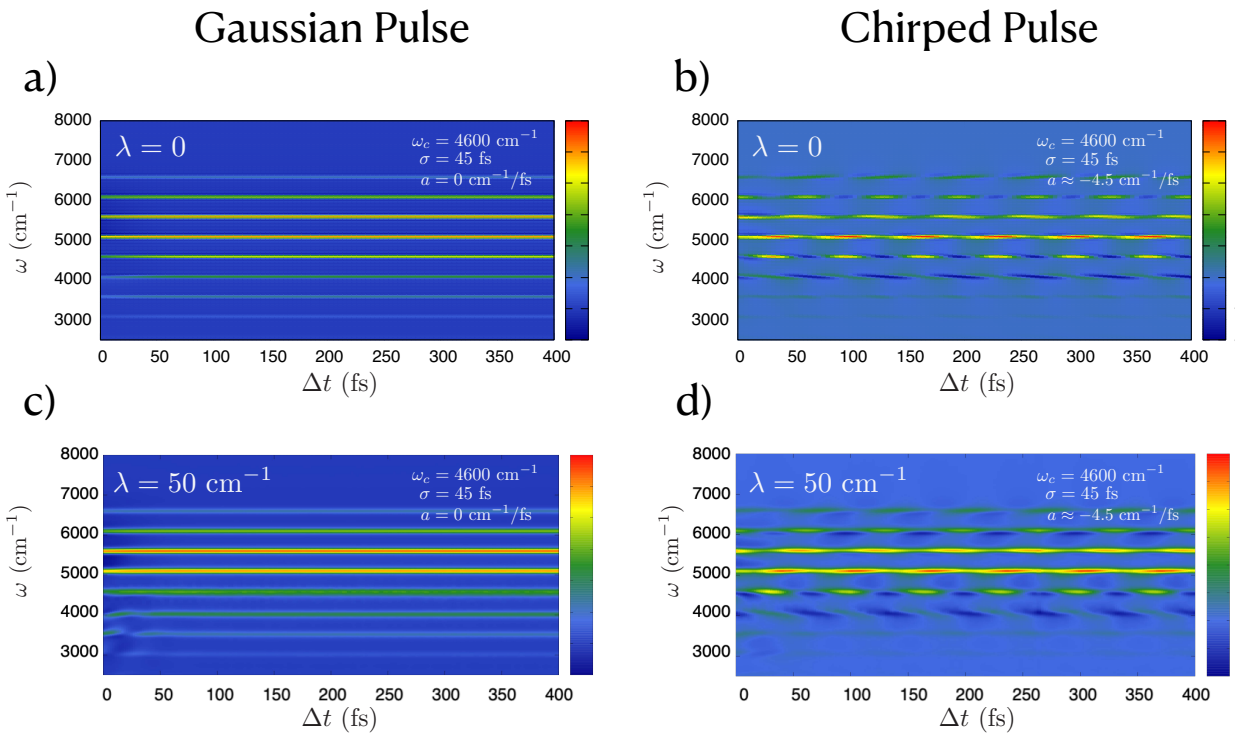

Figure 4: Pump-probe spectra for the shifted harmonic oscillator model described above. The spectra are obtained by Fourier transforming the nonlinear polarization that radiates in the $\mathbf{k}_2$ direction (see Figure 1) with respect to the time, τ, following an interaction with the probe pulse. The signals plotted here are then the negative of the imaginary part of these Fourier transformed results. Here, the left panels (a) and (c) represent the spectra produced when the Gaussian pulse with no chirp acts as the pump, while the right panels (b) and (d) show spectra obtained when the negatively chirped Gaussian pulse acts as the pump pulse. The Wigner spectrum and state preparation for each of these pulses are presented in Figure 3. The upper and lower sets of panels explore the influence of system-bath coupling strength, λ, on these spectra. The results presented here are obtained at a temperature of T=77 K.

of $\approx$ 66.7 fs). These simulations are representative of how the impact of shaped pulses on state preparation could manifest in experimental measurements of time-resolved pump-probe spectra.

The system-bath coupling incorporated in the model explored here includes only bath coupling to the electronic excitation and has the effect of simply broadening all the features in the pump-probe spectra. A model incorporating vibrational relaxation, on the other hand, would show evidence of excited wave packet relaxation dynamics that is not explored here.

5 Connecting with experiments

To better connect with experiments, where the pulse chirping is usually obtained by delaying certain frequency components with respect to others while keeping the shape of the original pulse in the frequency domain fixed,[6] we have performed a second scan over the chirp parameter (only) by imposing the constraint of identical frequency resolved field intensities $|E(\Omega)|^2$. The values for the final population produced by the chirped fields (in both the GS and ES), for a vibronic model with $\Omega = 500$ cm^{-1} and $S = 0.35$ are reported in Figure 5 and Table 1. The simulations were performed at T=300 K. At this temperature the first excited vibrational state of the ground electronic well is thermally populated ($\sim$8% according to the Boltzmann distribution): all the data presented hereafter are therefore obtained by performing simulations starting from both the ground and the first excited vibrational states of the ground electronic state, and summing the results with the proper Boltzmann weights. Even if in the present case the results are dominated by the 92% populated ground vibrational state, the same procedure may be applied to cases in which this effect may be important (e.g., when higher temperatures or modes with lower frequencies are considered). The equations for the chirped time-domain field parameters (i.e., the field strength λ_F and the pulse time-width σ_t, with the central frequency, ω_c, fixed at 5600 cm^{-1}), obtained by imposing the constraint outlined above that the pulses have the same shape in the frequency domain, as well as the Wigner maps of these pulses, are presented in the Supporting Information.

Some comments on the results of this constrained scan follow: (i) First of all we note that, due to the quadratic nature of the equations, for every chirp value, there are two fields with different shapes in the time domain (specified by λ_F and σ_t) that produce the same $|E(\Omega)|^2$. These solutions are labeled with subscripts S and L, corresponding to the shorter and longer pulse duration solutions, respectively. (ii) Table 1 reports the asymptotic populations for vibrationally cold/hot states in the electronic GS and ES, exploring the effect

[6] This means that different pulses have the same number of photons for each color, but, depending on the pulse chirp, the different colors arrive at the target at different times.

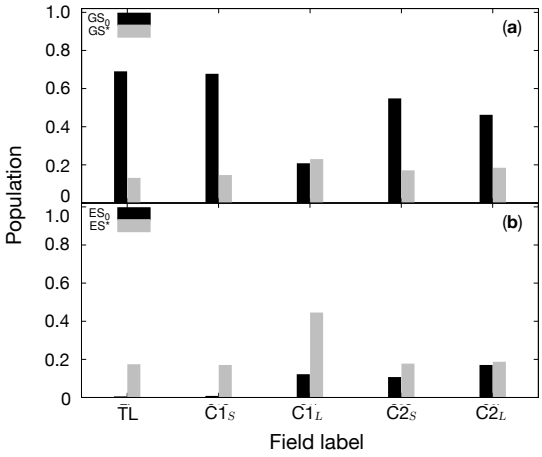

Figure 5: Column graph of the (a) GS and (b) ES population prepared by the different pulses. GS*/ES* (GS_0/ES_0) indicates vibrationally excited (cold) GS/ES population. Note that the $C1_L$ pulse changes the state preparation most significantly relative to the transform limited pulse. These results are obtained at T=300K.

of pulse chirping on the state preparation. The most remarkable change (with respect to the transform limited -TL- pulse) is observed in the case of $C1_L$, where, in contrast with all the other cases, the largest fraction of the population appears on the hot ES (and in particular around 30% in the first and 10% in the second excited vibrational levels); (iii) the bath does not seem to significantly influence these results, likely because the relaxation time used in the model is typically longer than the pulse duration.

In Figure 6 we present results of calculations in which we have simulated a pump-probe

Table 1: Influence of the chirp for state preparation experiments on the vibronic model introduced above. All the fields have the same frequency resolved intensity $|E(\Omega)|^2$. GS*/ES* (GS_0/ES_0) indicates vibrationally excited (cold) GS/ES population. The largest population values are in bold. The field parameters λ_F, σ_t and a are measured in cm^{-1}, fs, and cm^{-1}/fs, respectively. $^{(a)}$ The field strengths reported in the table have to be multiplied by 1500. All results presented here are obtained for temperature T=300K

	Field param.s			Pop.s ($\lambda = 0$)		Pop.s ($\lambda = 100$ cm^{-1})	
	$\lambda_F^{(a)}$	σ_t	a	GS* (GS_0)	ES* (ES_0)	GS* (GS_0)	ES* (ES_0)
TL	1.00	7.00	0	0.14 (**0.69**)	0.17 (0.01)	0.14 (**0.68**)	0.17 (0.02)
$C1_S$	0.99	7.14	-10.6	0.15 (**0.68**)	0.17 (0.01)	0.15 (**0.67**)	0.17 (0.02)
$C1_L$	0.45	34.99	-10.6	0.23 (0.21)	**0.45** (0.12)	0.21 (0.24)	**0.43** (0.12)
$C2_S$	0.88	9.04	-26.5	0.17 (**0.55**)	0.18 (0.11)	0.18 (**0.55**)	0.17 (0.11)
$C2_L$	0.80	11.06	-26.5	0.19 (**0.46**)	0.19 (0.17)	0.19 (**0.47**)	0.18 (0.17)

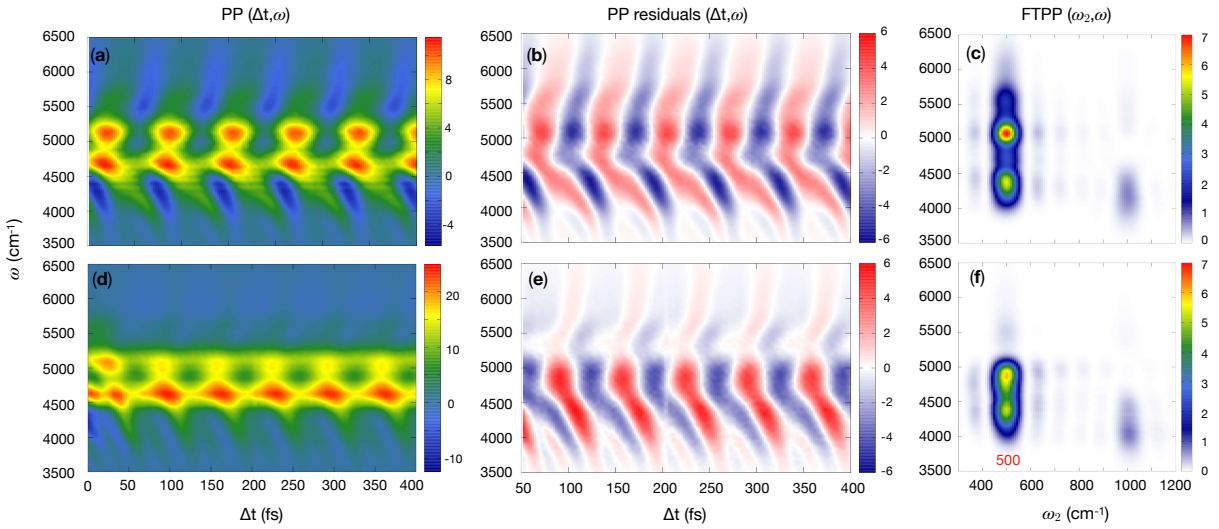

Figure 6: Pump-probe spectra produced by employing a TL probe pulse, with either (a) the TL or (d) the $C1_L$ chirped pulse as the pump. These spectra are computed in the same way as the results in Figure 4. The residual maps presented in panels (b) and (e), which highlight the oscillatory behavior of the PP data, are obtained by subtracting the Δt averaged signal for each value of ω from the plots in panels (a) and (d), respectively. Finally, we have Fourier transformed this residual data along Δt, and panels (c) and (f) plot the power spectra as the square modulus of this Fourier transformed residual data. The results presented here are for TL pump (panels (b) and (c)) and for the $C1_L$ pump (panels (e) and (f)). Results presented here are for T=300K. See text for details of the bath used in these studies.

experiment employing either TL (Figure 6 (a-c)) or $C1_L$ (Figure (d-f)) pump pulses, and an attenuated TL pulse as probe (the TL probe pulse intensity was reduced to 20% of the original intensity). A bath with $\lambda = 100$ cm^{-1} and $\gamma^{-1} = 50$ fs was coupled to the system. We have further analyzed the pump-probe spectra by visualizing the oscillating residuals (obtained by subtracting, for each detection frequency ω, the constant contributions - Figure 6 (b) and (e)), and by means of the so-called power-spectrum, which is the square modulus of the Fourier transform of the residual map along the time coordinate Δt, which becomes an additional frequency axis (labeled ω_2 - Figure 6 (c) and (f)). This pump-probe spectrum captures the beating frequencies along the delay time between pump and probe, and as such can monitor the ability of the pump pulse to create oscillatory wave-packets in either the ground or excited electronic state. The beating frequency is expected to reveal the wave-packet dynamics of molecular modes that are strongly coupled to the observed excited state:

in this case the 500 cm^{-1} mode and possible overtones. From the calculated model pump-probe spectra presented in Figure 6, it is clear that the different initial states prepared by using either TL or $C1_L$ as pump pulses, result in significant differences in the pump-probe signals. We note in particular that $C1_L$ quenches the signals above 5300 cm^{-1}. Moreover, the nodal structure of the pump-probe map, which is used in experiments to track (for example) dynamical Stokes shift effects, is modified by the use of the chirp pump.

These results demonstrate the ability to use chirped pulses to control the initial state preparation of a vibronic system, and show that the state preparation process is robust to the bath induced fluctuations (at least when the bath relaxation time is longer than the pulse duration). Moreover these simulations suggest that the different prepared states, can be monitored in pump-probe experiments, which are demonstrated to be sensitive to the initial (pump-produced) state. Future studies will explore (i) the state-preparation/chirp/noise relationships and (ii) the effect of using chirp-pulses in pump-probe spectroscopy by detailed comparison of experimental results and theoretical predictions for model molecular systems.[49]

6 Conclusions and Future Directions

Here, the general formalism for computing explicit field-matter interactions within the PLDM formalism is presented. Employing simple models, we have shown that this formalism can be used to design (and eventually optimize) field-matter interactions to enhance selected quantum processes. We report results of a scan over field parameters for a simple one-dimensional spin-boson model interacting with an incident radiation field and demonstrate how the optimal field for producing a desired state of a model condense phase system could be determined. We explore how the fidelity of state targeting is influenced by characteristics of the system-bath coupling in this model.

A discussion of how one can obtain nonlinear spectroscopic signals through non-perturbative

field-matter interactions was presented,[40] and the pump-probe signal was computed for a spin-boson model with the PLDM algorithm. These preliminary results show the impact of different pulse shapes and sequences on spectroscopic observables, and serve as a starting point for the implementation of the PLDM algorithm in the context of quantum optimal control theory.[2,50] While the results presented here are restricted to the driving of electronic / vibronic transitions, more general field-matter interactions can also be considered. For example, one could consider infrared pulse sequences, as has been studied in the context of nonlinear infrared spectroscopies with the intimately-related mixed quantum-classical Liouville equation.[51–53]

Finally, to better connect with experiments, the ability to use different chirped pulses, characterized by identical intensity profiles in the frequency space, to control vibronic state preparation has been tested on a second model system. The relationship between state preparation controllability, pulse properties and external noise (bath properties, such as the strength of system-bath coupling and its characteristic relaxation time[1]) should be explored experimentally and theoretically.[49]

Future work in this direction will involve the use of higher-dimensional *ab-initio* parameterized models of molecular systems for designing optimal pulse sequences through simulations,[50] as well as understanding the dynamical mechanisms underlying experimentally-determined optimal control sequences.[9,10]

7 Acknowledgements

We acknowledge support for this research from the US Department of Energy, Office of Basic Energy Sciences under contract DE-SC0020437, and from the National Science Foundation under grant CHE-1955407. We acknowledge discussions with Prof. Greg Scholes and preliminary experimental results from Ms. Catrina Oberg, which provided important motivation for the theoretical developments presented here.

8 Supporting Information

The following sections are available in the Supporting Information: (1) Justification of RWA in this application, (2) Wigner spectrum of electromagnetic field, (3) PLDM field-driven method vs exact calculations, (4) How to prepare chirped pulses with fixed $|E(\Omega)|^2$, (5) Heat maps for ground state vibrational excitation as a function of driving chirped pulse field parameters with different carrier frequencies, and (6) Comparison of pump-probe spectra of the simple harmonic model at T = 77K and T = 300K. This information is available free of charge via the Internet at http://pubs.acs.org.

References

(1) McRobbie, P. L.; Geva, E. Coherent Control of Population Transfer via Linear Chirp in Liquid Solution: The Role of Motional Narrowing. *J. Phys. Chem. A* **2015**, *120*, 3015–3022.

(2) Rabitz, H.; de Vivie-Riedle, R.; Motzkus, M.; Kompa, K. Whither the Future of Controlling Quantum Phenomena? *Science* **2000**, *288*, 824–828.

(3) Brüggemann, B.; May, V. Ultrafast Laser Pulse Control of Exciton Dynamics: A Computational Study on the FMO Complex. *J. Phys. Chem. B* **2004**, *108*, 10529–10539.

(4) Petersen, J.; Wohlgemuth, M.; Sellner, B.; Bonačić-Koutecký, V.; Lischka, H.; Mitrić, R. Laser Pulse Trains for Controlling Excited State Dynamics of Adenine in Water. *Phys. Chem. Chem. Phys.* **2012**, *14*, 4687–4694.

(5) Christopher, P.; Shapiro, M.; Brumer, P. Quantum Control of Internal Conversion in 24-Vibrational-Mode Pyrazine. *J. Chem. Phys.* **2006**, *125*, 124310.

(6) Gerbasi, D.; Sanz, A.; Christopher, P.; Shapiro, M.; Brumer, P. Overlapping Resonances

in the Control of Intramolecular Vibrational Redistribution. *J. Chem. Phys.* **2007**, *126*, 124307.

(7) Judson, R. S.; Rabitz, H. Teaching Lasers to Control Molecules. *Phys. Rev. Lett.* **1992**, *68*, 1500.

(8) Bardeen, C. J.; Yakovlev, V. V.; Squier, J. A.; Wilson, K. R. Quantum Control of Population Transfer in Green Fluorescent Protein by using Chirped Femtosecond Pulses. *J. Am. Chem. Soc.* **1998**, *120*, 13023–13027.

(9) Dietzek, B.; Brüggemann, B.; Pascher, T.; Yartsev, A. Mechanisms of Molecular Response in the Optimal Control of Photoisomerization. *Phys. Rev. Lett.* **2006**, *97*, 258301.

(10) Prokhorenko, V. I.; Nagy, A. M.; Waschuk, S. A.; Brown, L. S.; Birge, R. R.; Miller, R. D. Coherent Control of Retinal Isomerization in Bacteriorhodopsin. *Science* **2006**, *313*, 1257–1261.

(11) Gelin, M. F.; Egorova, D.; Domcke, W. Manipulating Electronic Couplings and Nonadiabatic Nuclear Dynamics with Strong Laser Pulses. *J. Chem. Phys.* **2009**, *131*, 124505.

(12) Savolainen, J.; Fanciulli, R.; Dijkhuizen, N.; Moore, A. L.; Hauer, J.; Buckup, T.; Motzkus, M.; Herek, J. L. Controlling the Efficiency of an Artificial Light-Harvesting Complex. *Proc. Natl. Acad. Sci. U. S. A.* **2008**, *105*, 7641–7646.

(13) Cheng, Y.-C.; Fleming, G. R. Coherence Quantum Beats in Two-Dimensional Electronic Spectroscopy. *J. Phys. Chem. A* **2008**, *112*, 4254–4260.

(14) Dean, J. C.; Mirkovic, T.; Toa, Z. S.; Oblinsky, D. G.; Scholes, G. D. Vibronic Enhancement of Algae Light Harvesting. *Chem* **2016**, *1*, 858–872.

(15) Chenu, A.; Scholes, G. D. Coherence in Energy Transfer and Photosynthesis. *Annu. Rev. Phys. Chem.* **2015**, *66*, 69–96.

(16) Arpin, P. C.; Turner, D. B.; McClure, S. D.; Jumper, C. C.; Mirkovic, T.; Challa, J. R.; Lee, J.; Teng, C. Y.; Green, B. R.; Wilk, K. E.; Curmi, P. M. G.; Hoef-Emden, K.; McCamant, D. W.; Scholes, G. D. Spectroscopic Studies of Cryptophyte Light Harvesting Proteins: Vibrations and Coherent Oscillations. *J. Phys. Chem. B* **2015**, *119*, 10025–10034.

(17) Maiuri, M.; Ostroumov, E. E.; Saer, R. G.; Blankenship, R. E.; Scholes, G. D. Coherent Wavepackets in the Fenna–Matthews–Olson Complex are Robust to Excitonic-Structure Perturbations Caused by Mutagenesis. *Nat. Chem.* **2018**, *10*, 177.

(18) Grinev, T.; Brumer, P. Realistic vs Sudden Turn-on of Natural Incoherent Light: Coherences and Dynamics in Molecular Excitation and Internal Conversion. *J. Chem. Phys.* **2015**, *143*, 244313.

(19) Mukamel, S. *Principles of Nonlinear Optical Spectroscopy*; Oxford University Press, New York, 1995; Vol. 29.

(20) Abramavicius, D.; Palmieri, B.; Voronine, D. V.; Sanda, F.; Mukamel, S. Coherent Multidimensional Optical Spectroscopy of Excitons in Molecular Aggregates; Quasiparticle Versus Supermolecule Perspectives. *Chem. Rev.* **2009**, *109*, 2350–2408.

(21) Segatta, F.; Cupellini, L.; Jurinovich, S.; Mukamel, S.; Dapor, M.; Taioli, S.; Garavelli, M.; Mennucci, B. A Quantum Chemical Interpretation of Two-Dimensional Electronic Spectroscopy of Light-Harvesting Complexes. *J. Am. Chem. Soc.* **2017**, *139*, 7558–7567.

(22) Gao, X.; Geva, E. A Nonperturbative Methodology for Simulating Multidimensional Spectra of Multiexcitonic Molecular Systems via Quasiclassical Mapping Hamiltonian Methods. *J. Chem. Theory Comput.* **2020**, *16*, 6491–6502.

(23) Gao, X.; Lai, Y.; Geva, E. Simulating Absorption Spectra of Multiexcitonic Systems

via Quasiclassical Mapping Hamiltonian Methods. *J. Chem. Theory Comput.* **2020**, *16*, 6465–6480.

(24) Huo, P.; Coker, D. F. Communication: Partial Linearized Density Matrix Dynamics for Dissipative, Non-Adiabatic Quantum Evolution. *J. Chem. Phys.* **2011**, *135*, 201101.

(25) Lee, M. K.; Huo, P.; Coker, D. F. Semiclassical Path Integral Dynamics: Photosynthetic Energy Transfer with Realistic Environment Interactions. *Annu. Rev. Phys. Chem.* **2016**, *67*, 639–668.

(26) Huo, P.; Miller, T. F.; Coker, D. F. Communication: Predictive Partial Linearized Path Integral Simulation of Condensed Phase Electron Transfer Dynamics. *J. Chem. Phys.* **2013**, *139*, 151103.

(27) Provazza, J.; Segatta, F.; Garavelli, M.; Coker, D. F. Semiclassical Path Integral Calculation of Nonlinear Optical Spectroscopy. *J. Chem. Theory Comput.* **2018**, *14*, 856–866.

(28) Mandal, A.; Huo, P. Investigate New Reactivities Enabled by Polariton Photochemistry. **2019**,

(29) Mannouch, J. R.; Richardson, J. O. A Partially Linearized Spin-Mapping Approach for Nonadiabatic Dynamics. I. Derivation of the Theory. *arXiv preprint arXiv:2007.05047* **2020**,

(30) Mannouch, J. R.; Richardson, J. O. A Partially Linearized Spin-Mapping Approach for Nonadiabatic Dynamics. II. Analysis and Comparison with Related Approaches. *arXiv preprint arXiv:2007.05048* **2020**,

(31) Meyer, H.-D.; Miller, W. H. A Classical Analog for Electronic Degrees of Freedom in Nonadiabatic Collision Processes. *J. Chem. Phys.* **1979**, *70*, 3214–3223.

(32) Stock, G.; Thoss, M. Semiclassical Description of Nonadiabatic Quantum Dynamics. *Phys. Rev. Lett.* **1997**, *78*, 578–581.

(33) Thoss, M.; Stock, G. Mapping Approach to the Semiclassical Description of Nonadiabatic Quantum Dynamics. *Phys. Rev. A* **1999**, *59*, 64.

(34) Schatz, G. C.; Ratner, M. A. *Quantum Mechanics in Chemistry*, dover ed.; Dover, 2002.

(35) Polkovnikov, A. Phase Space Representation of Quantum Dynamics. *Ann. Phys.* **2010**, *325*, 1790–1852.

(36) Bonella, S.; Coker, D. F. LAND-map, a Linearized Approach to Nonadiabatic Dynamics using the Mapping Formalism. *J. Chem. Phys.* **2005**, *122*, 194102.

(37) Trebino, R.; DeLong, K. W.; Fittinghoff, D. N.; Sweetser, J. N.; Krumbügel, M. A.; Richman, B. A.; Kane, D. J. Measuring Ultrashort Laser Pulses in the Time-Frequency Domain using Frequency-Resolved Optical Gating. *Rev. Sci. Instrum.* **1997**, *68*, 3277–3295.

(38) Diels, J.-C.; Rudolph, W. *Ultrashort Laser Pulse Phenomena*; Elsevier, 2006.

(39) Segarra-Martí, J.; Segatta, F.; Mackenzie, T. A.; Nenov, A.; Rivalta, I.; Bearpark, M. J.; Garavelli, M. Modeling Multidimensional Spectral Lineshapes from First Principles: Application to Water-Solvated Adenine. *Faraday Discuss.* **2019**, *221*, 219–244.

(40) Seidner, L.; Stock, G.; Domcke, W. Nonperturbative Approach to Femtosecond Spectroscopy: General Theory and Application to Multidimensional Nonadiabatic Photoisomerization Processes. *J. Chem. Phys.* **1995**, *103*, 3998–4011.

(41) Martinez, F.; Rekik, N.; Hanna, G. Simulation of Nonlinear Optical Signals via Approximate Solutions of the Quantum-Classical Liouville Equation: Application to the Pump-Probe Spectroscopy of a Condensed Phase Electron Transfer Reaction. *Chem. Phys. Lett.* **2013**, *573*, 77–83.

(42) Mančal, T.; Pisliakov, A. V.; Fleming, G. R. Two-Dimensional Optical Three-Pulse

Photon Echo Spectroscopy. I. Nonperturbative Approach to the Calculation of Spectra. *J. Chem. Phys.* **2006**, *124*, 234504.

(43) Gelin, M. F.; Egorova, D.; Domcke, W. Efficient Method for the Calculation of Time- and Frequency-Resolved Four-Wave Mixing Signals and its Application to Photon-Echo Spectroscopy. *J. Chem. Phys.* **2005**, *123*, 164112.

(44) Egorova, D.; Gelin, M. F.; Domcke, W. Analysis of Cross Peaks in Two-Dimensional Electronic Photon-Echo Spectroscopy for Simple Models with Vibrations and Dissipation. *J. Chem. Phys.* **2007**, *126*, 074314.

(45) Cheng, Y.-C.; Engel, G. S.; Fleming, G. R. Elucidation of Population and Coherence Dynamics using Cross-Peaks in Two-Dimensional Electronic Spectroscopy. *Chem. Phys.* **2007**, *341*, 285–295.

(46) Tempelaar, R.; Stradomska, A.; Knoester, J.; Spano, F. C. Anatomy of an Exciton: Vibrational Distortion and Exciton Coherence in H- and J-Aggregates. *J. Phys. Chem. B* **2013**, *117*, 457–466.

(47) Bašinskaitė, E.; Butkus, V.; Abramavicius, D.; Valkunas, L. Vibronic Models for Nonlinear Spectroscopy Simulations. *Photosynth. Res.* **2014**, *121*, 95–106.

(48) Ruhman, S.; Kosloff, R. Application of Chirped Ultrashort Pulses for Generating Large-Amplitude Ground-State Vibrational Coherence: A Computer Simulation. *J. Opt. Soc. Am. B* **1990**, *7*, 1748–1752.

(49) Oberg, C.; Segatta, F.; Provazza, J. A.; Scholes, G. D.; Coker, D. F. Control of Vibronic State Preparation using Chirped Pulses in Nonlinear Spectroscopy. *Manuscript in preparation* **2020**,

(50) Shapiro, M.; Brumer, P. Principles of the Quantum Control of Molecular Processes.

Principles of the Quantum Control of Molecular Processes, by Moshe Shapiro, Paul Brumer, pp. 250. ISBN 0-471-24184-9. Wiley-VCH, February 2003. **2003**, 250.

(51) Hanna, G.; Geva, E. Signature of Nonadiabatic Transitions on the Pump-Probe Infrared Spectra of a Hydrogen-Bonded Complex Dissolved in a Polar Solvent: A Computational Study. *J. Phys. Chem. B* **2011**, *115*, 5191–5200.

(52) Hanna, G.; Geva, E. Multidimensional Spectra via the Mixed Quantum-Classical Liouville Method: Signatures of Nonequilibrium Dynamics. *J. Phys. Chem. B* **2009**, *113*, 9278–9288.

(53) Kwac, K.; Geva, E. A Mixed Quantum-Classical Molecular Dynamics Study of the Hydroxyl Stretch in Methanol/Carbon Tetrachloride Mixtures III: Nonequilibrium Hydrogen-Bond Dynamics and Infrared Pump–Probe Spectra. *J. Phys. Chem. B* **2013**, *117*, 7737–7749.

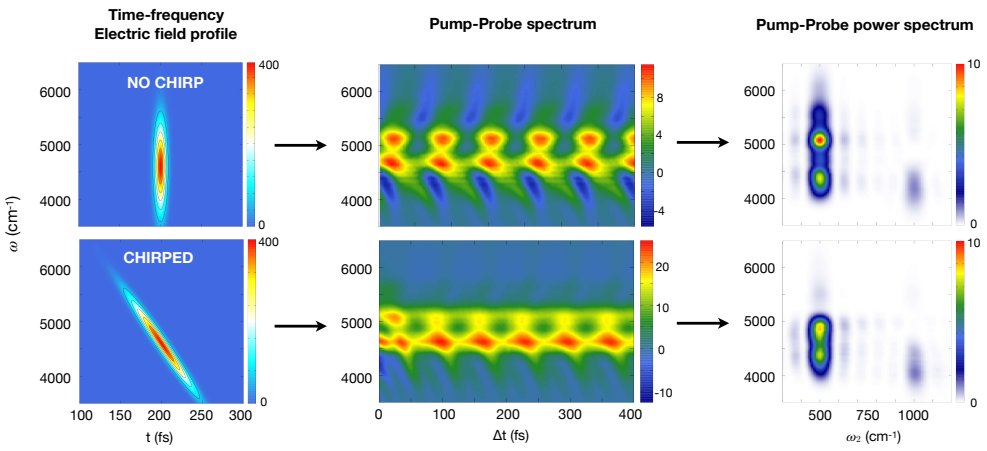

Figure 7: Table of Contents Figure